

# Boltzmann Attention Sampling for Image Analysis with Small Objects

Theodore Zhao\*    Sid Kiblawi\*    Naoto Usuyama    Ho Hin Lee  
 Sam Preston    Hoifung Poon    Mu Wei†  
 Microsoft, Redmond, WA, USA  
<https://aka.ms/boltzformer>

## Abstract

*Detecting and segmenting small objects, such as lung nodules and tumor lesions, remains a critical challenge in image analysis. These objects often occupy less than 0.1% of an image, making traditional transformer architectures inefficient and prone to performance degradation due to redundant attention computations on irrelevant regions. Existing sparse attention mechanisms rely on rigid hierarchical structures, which are poorly suited for detecting small, variable, and uncertain object locations. In this paper, we propose BoltzFormer, a novel transformer-based architecture designed to address these challenges through dynamic sparse attention. BoltzFormer identifies and focuses attention on relevant areas by modeling uncertainty using a Boltzmann distribution with an annealing schedule. Initially, a higher temperature allows broader area sampling in early layers, when object location uncertainty is greatest. As the temperature decreases in later layers, attention becomes more focused, enhancing efficiency and accuracy. BoltzFormer seamlessly integrates into existing transformer architectures via a modular Boltzmann attention sampling mechanism. Comprehensive evaluations on benchmark datasets demonstrate that BoltzFormer significantly improves segmentation performance for small objects while reducing attention computation by an order of magnitude compared to previous state-of-the-art methods.*

## 1. Introduction

Transformer [24] has significantly changed the field of image analysis. Its attention-based architecture introduces flexibility in handling inputs from various modalities, including images, text, and other forms of prompts. Seminal works such as SAM [14], SAM 2 [20], and SEEM [33] unify segmentation tasks for various object types, making the models flexible and generalizable. There is also rising

interest in adapting such promptable segmentation models to key application domains, such as biomedicine (e.g., MedSAM [17], BiomedParse [29], and MedSAM-2 [30]).

While the progress is exciting, challenges abound. A salient growth area is small objects, which are particularly difficult for conventional segmentation models, especially when there is no user-provided bounding box and only the object description is available as input [7, 29]. This challenge is especially pronounced in critical application domains such as biomedicine, when important objects like lung nodules, tumor lesions, vessels, and many other anatomical structures are tiny, sometimes occupying less than 0.1% of the image. By default, many standard segmentation models require the user to conduct the object detection step and provide object-specific spatial prompts as input, such as bounding boxes, points, or scribbles [15, 17, 25, 30]. In many applications, there are a large number of objects and this approach is clearly not scalable. Ideally, a user can simply specify the object description in a text prompt, and the model can automatically detect and segment the given objects, as in BiomedParse [29]. However, in such an end-to-end setting, small objects pose significant challenges because they are particularly hard to locate and identify.

The difficulty in detecting and segmenting small objects originates from the nature of the attention mechanism in transformer. For a small object, the relevant information is confined within a tiny portion of the image (the object and its neighborhood). This means that the vast majority of attention computation would be spent on irrelevant pixels far away from the object. In addition to being wasteful, this also introduces significant distractions and noises, making the learning less efficient. Prior work has attempted to address this issue by focusing decoding on the foreground regions [7, 28]. However, they used relatively rigid rules, which are ill-suited for small objects due to their variability and the uncertainty about their locations.

In this paper, we propose a novel transformer architec-

\*Equal contribution.

†Corresponding authors.

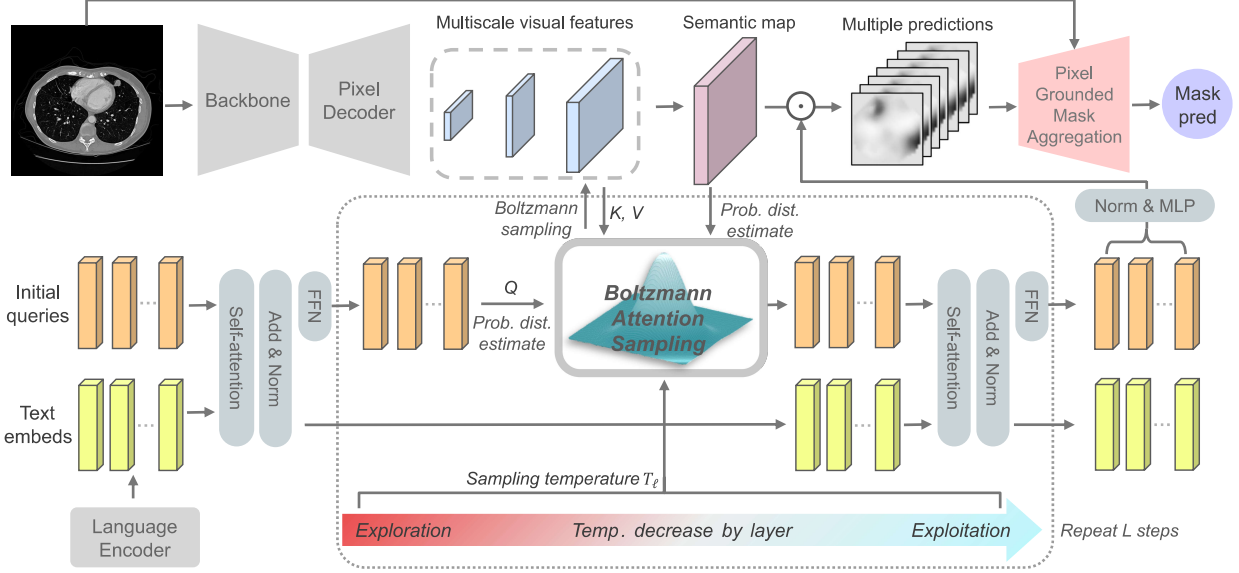


Figure 1. The overall architecture of *BoltzFormer* for end-to-end object detection and segmentation via a unified text prompt. *BoltzFormer* is a novel transform-based architecture that introduces a Boltzmann attention sampling module to dynamically propose sparse areas to focus cross-attention in each layer using a Boltzmann distribution. To account for uncertainty, which is especially high in earlier stage of computation, *BoltzFormer* starts with a high temperature in the first layer, which gradually cools down in subsequent layers. This is reminiscent of a reinforcement learning process, where exploration is favored in the initial layers (more sparse areas being sampled), and exploitation in later layers (focusing on a handful of most promising areas). The model takes image (upper left) and text prompt (lower left) as input, and outputs segmentation mask (upper right) for the object specified in the text prompt. Specifically, we use a standard image encoder to obtain multiscale visual features, including a high-resolution semantic map (upper middle). *BoltzFormer* starts with a set of latent queries that try to model the correct semantic for the prompted object in the image (middle left). In each layer, the query vectors are combined with the semantic map to produce a Boltzmann distribution over the image, which is then used to sample the sparse areas. They each attend exclusively to the visual features in the sampled area and update themselves (see Figure 2 for more details). The queries communicate with the text embeddings through self-attention after each Boltzmann attention sampling layer (center block). After the transformer layers, each query is combined with the image semantic map to generate a candidate predicted mask. The predictions are aggregated by a pixel grounded mask aggregation (PiGMA) module into the final mask prediction (upper right, see Figure 3 for details).

ture, *BoltzFormer*, which learns to use a Boltzmann distribution to dynamically propose sparse candidate areas to focus attention computation on. *BoltzFormer* takes an image and a natural-language description as input and conducts end-to-end detection and segmentation of the object as specified by the text prompt, as illustrated in Fig. 1. To accommodate uncertainty about the object location, *BoltzFormer* employs an annealing schedule, which starts with a high temperature for the Boltzmann distribution so that it would propose more areas to sample when the uncertainty is the highest, and cools down in subsequent layers as the object location becomes clearer so that the model can focus on identifying the details in the object segment. The Boltzmann sampling step is modular and can be easily incorporated into any modern transformer-based image analysis process.

We develop a reference system for *BoltzFormer* by combining the Boltzmann sampling module with state-of-the-art design for end-to-end image analysis. Specifically, we use a state-of-the-art image encoder to extract multi-scale visual

features and a semantic map, and learn a set of latent query vectors in tandem with the image representation and text embedding. The learning is unrolled in a deep architecture with transformer-based layers augmented by the Boltzmann attention sampling module. In the final layer, the query vectors are combined with the image representation to generate candidate segmentation masks, which are aggregated by a Pixel Grounded Mask Aggregation (PiGMA) module to produce the final segmentation mask output.

We highlight our contributions as follows:

- To the best of our knowledge, we are the first to incorporate Boltzmann sampling into transformer to focus attention computation on sparse areas of the image that most likely contain the queried object. We conducted thorough ablation studies to establish the best practice for this novel transformer architecture.
- We propose a novel PiGMA module to efficiently aggregate an ensemble of segmentation mask predictions based on the query vectors. Through ablation studies, we demonstrate the effectiveness of this ensemble approach.

- We conducted extensive evaluation on end-to-end object segmentation via a text prompt, using challenging segmentation datasets with objects of size ranging from 0.002%-20% of the image. Remarkably, *BoltzFormer* substantially outperforms prior best methods, attaining a gain of 3-12 absolute points in mean Dice score, while reducing attention computation by an order of magnitude.

## 2. Related work

Segmentation and detection have been the core parts of image analysis, especially in medical images. Architecture wise, the field witnesses the progress from convolutional neural networks (CNNs), particularly architectures like Fast R-CNN [9], U-Net [21], Mask R-CNN [10] and Sparse R-CNN [23] to recent development of transformers. This transformer revolution led to seminal works including DETR [5], MaskFormer [6], and Mask2Former [7]. All these works used transformer decoder as the unifying architecture.

These transformer decoder for segmentation and detection nourished the recent developments toward generalized promptable image segmentation models, including Segment Anything Model (SAM) [14], SAM 2 [20], and Segment Everything Everywhere Model (SEEM) [33]. All these models feature a transformer mask decoder with flexibility in taking prompts such as points, bounding boxes and text. While the image encoder and prompt encoder are flexibly chosen, the transformer mask decoder plays the critical role in performing quality segmentation. The decoders of SAM and SAM 2 were derived from MaskFormer [6], and SEEM was built upon the Mask2Former [7] architecture. Our work aims to improve upon the above mentioned transformer mask decoder architectures in the text prompting scenario.

There have been several advances in biomedical segmentation by utilizing the architectures presented above and training them with more biological focused data. MedSAM [17] was finetuned on SAM using a large-scale dataset of over 1.5 million image-mask pairs across 10 imaging modalities and 30 cancer types, demonstrating superior segmentation performance and adaptability compared to modality-specific models. MedSAM 2 [18] extends MedSAM to 3D medical imaging, supporting segmentation in volumetric and time-sequential data. BiomedParse [29], built upon SEEM, is a biomedical foundational model in that unifies segmentation, detection, and recognition tasks. By using text prompts, BiomedParse removes manual bounding-box interactions and enables scalable and accurate segmentation. In evaluations, BiomedParse outperformed state-of-the-art models, particularly for objects with complex and irregular shapes. However, finding small objects with text prompt is still a challenge.

In order to improve segmentation performance, re-

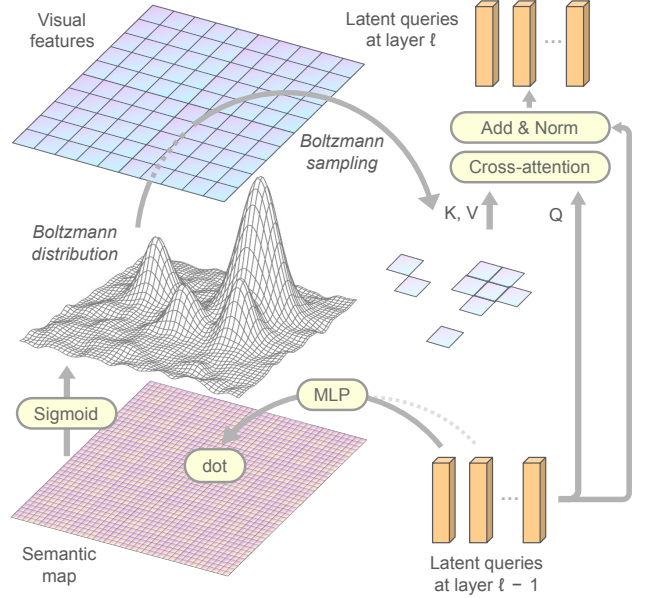


Figure 2. Illustration of the Boltzmann attention sampling block (center block in Fig. 1). The latent queries from the previous layer each goes through the MLP transformation (Eq. (3)) with dimension kept constant. Each transformed query vector takes dot product with all feature vectors on the semantic map, yielding scalars on the map. We use sigmoid to transform the scores into (0,1), and compute the Boltzmann distribution of temperature  $\tau_\ell$  using Eq. (5). We then draw from the distribution to sample the corresponding patches in the visual feature for  $N$  trials with replacement. The query attends exclusively to the samples features and add to itself. We perform the same for all query vectors and apply layer normalization on them at the end.

searchers have developed attention masking techniques. One closely approach is in Mask2Former [7], where the masked attention operation is hard thresholded by the previous layer’s prediction. However, the prediction is not consistent across the layers, and the model struggles with small objects. MP-Former [28] proposed to introduce ground truth mask with point noise during training, however, the distribution difference between training and inference amplifies the inference time error, which is severe for small objects. In contrast, the proposed Boltzmann attention sampling uses probabilistic sampling to promote identifying the right regions throughout all layers. We compared our Boltzmann sampling strategy with the fixed threshold technique in ablation studies.

The proposed Boltzmann attention sampling shares similarity with several approaches aimed at making transformers effective for handling long sequences [3, 8]. However, the proposed method is fundamentally different in that the Boltzmann sampling is done prior to the standard full attention, whereas methods for long sequences directly modify the full attention computation. Conceptually, attention-

for-long-sequence methods sample to approximate where as the proposed method sample to focus. In computer vision, Deformable DETR [31] reduces computation by focusing on a deformable neighbor around a reference point, achieving sparsity but more in a deformable convolution fashion. Most of these works typically rely on fixed patterns, while *BoltzFormer* learns a spatial probability distribution and selects in a stochastic manner.

### 3. Method

The overall architecture of our model is illustrated in Figure 1. *BoltzFormer* is a transformer decoder that takes in image features from an image encoder (upper left) and text embeddings from a language encoder (lower left). The output is a binary segmentation mask (upper right) corresponding to the text prompt. The core component is the Boltzmann attention sampling block (center) to be described in details.

#### 3.1. Problem Setup

We formulate the problem as pixel-wise binary classification (pixel belongs to the text prompt semantics or not). We encode the input image using a backbone followed by a pixel decoder following [7], resulting in visual features  $\mathbf{V}^{(\lambda)} \in \mathbb{R}^{\frac{H}{\lambda} \times \frac{W}{\lambda} \times d}$  with different down-sampling factors  $\lambda$ . A semantic map  $\mathbf{S} \in \mathbb{R}^{H \times W \times d}$  is derived from the multi-scale visual features to represent the unified image semantics. The text prompt is encoded into a sequence of embeddings  $\mathbf{T} \in \mathbb{R}^{N_T \times d}$ . We classify each pixel  $(x, y)$  with

$$U_{xy}(\mu) = \text{sigmoid}(\mu^T \mathbf{S}_{xy}), \quad (1)$$

where the  $\mu \in \mathbb{R}^d$  vector is found by *BoltzFormer* as a function  $\mathcal{B}$  of the image and text features

$$\mu = \mathcal{B}(\mathbf{V}, \mathbf{S}, \mathbf{T}). \quad (2)$$

Below we show how *BoltzFormer* finds a good  $\mu$  vector based on the image and text features.

#### 3.2. BoltzFormer

*BoltzFormer* finds the  $\mu$  vector by finding a latent query vector  $q \in \mathbb{R}^d$ , which maps to  $\mu$  through a nonlinear MLP transformation

$$\mu = \text{MLP}(q). \quad (3)$$

Instead of using a single latent query vector  $q$ , we initiate an ensemble of  $m$  queries, forming  $\mathbf{Q} = [q^{(1)}, \dots, q^{(m)}]$ . Each query yields its own prediction at the end. The ensemble reduce uncertainty as Boltzmann sampling is a stochastic process, and also communicate among themselves.

##### 3.2.1. Text-conditioned prior

Prior to taking any input from the image, we start the latent query  $\mathbf{Q}_0$  by conditioning on the text embedding  $\mathbf{T}$ :

$$\mathbf{Q}_0 = \text{FFN}(\text{LayerNorm}([\mathbf{Q}, \mathbf{T}] + \text{SelfAttn}[\mathbf{Q}, \mathbf{T}])), \quad (4)$$

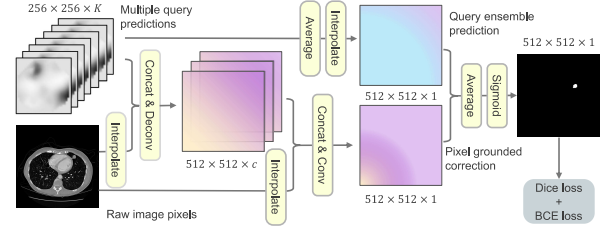


Figure 3. The architecture of the PiGMA module. The module takes in the predictions from the final layer queries. The query ensemble prediction part (top row) simply averages the predictions and interpolates to higher resolution. The pixel grounded correction part (de)convolves the predictions twice into higher resolution. In each convolution layer, we feed in the resized original image and concatenate on the channel dimension.  $c$  is the intermediate convolution dimension. Finally, the query ensemble prediction and pixel grounded correction are averaged and passed through a sigmoid transformation to produce the pixel-wise probability mask prediction.

where  $\mathbf{Q}$  is the learnable initial query matrix. We concatenate  $[\mathbf{Q}, \mathbf{T}]$  before performing self-attention, and split out only the  $\mathbf{Q}$  part before the feed-forward network layer FFN. The same operation applies to following  $[\mathbf{Q}, \mathbf{T}]$  self-attention blocks.

##### 3.2.2. Boltzmann Attention Sampling

The latent queries then go through  $L$  layers of *BoltzFormer* blocks (big box in the lower center of Fig. 1). The core in each block is the Boltzmann attention sampling unit (center small box in Fig. 1 and the whole Fig. 2) where the queries  $\mathbf{Q}_\ell$  sample information from the visual features to update themselves. Each Boltzmann attention sampling unit is followed by a self-attention layer for the queries to attend to each other and to the text embeddings. The steps are described in details below.

**Step 1. Boltzmann distribution** Given the query  $q_\ell^{(i)}$  at layer  $\ell$ , we first use it to compute the Boltzmann distribution on the image, which is a probability field

$$p_{xy}(q_\ell^{(i)}) = \frac{\exp(U_{xy}(\text{MLP}(q_\ell^{(i)}))/\tau_\ell)}{\int_{x'y'} \exp(U_{x'y'}(\text{MLP}(q_\ell^{(i)}))/\tau_\ell)}. \quad (5)$$

Here we apply the same MLP transformation in Eq. (3), and the pixel confidence estimator Eq. (1). The integral is on all  $(x', y')$  on the image field to normalize the distribution. Note that we use a continuous form here to efficiently consider different scales of image features. The discrete distribution can be easily obtained through grid interpolation in real implementation.

Based on Eq. (5), areas with higher confidence scores  $U_{xy}$  are assigned higher sampling probabilities. The sam-



pling temperature  $\tau_\ell$  controls the concentration of the distribution in high-confidence areas. As layer  $\ell$  increases, we gradually decrease the temperature according to  $\tau_\ell = \tau_0/(1 + \ell)$ , where  $\tau_0$  is the temperature at the base layer  $\ell = 0$ . As illustrated at the bottom of Figure 1, we encourage exploration across the entire image in the early layers and progressively shift towards exploitation of the most confident regions.

**Step 2. Random attention sampling** We then sample from the visual feature  $\mathbf{V}^{(\lambda)}$  according to the Boltzmann distribution  $p_{xy}(q_\ell^{(i)})$  estimated by query  $q_\ell^{(i)}$ . (In each layer we use one of the visual feature scales  $\lambda$ . We leave it to the implementation details in appendix.) As  $\mathbf{V}^{(\lambda)}$  forms a down-sampled grid on the image, we first interpolate  $p_{xy}(q_\ell^{(i)})$  to assign probability for each patch. We draw from the distribution over the patches for  $N$  independent trials<sup>1</sup>. The union of the sampled patches forms an attention set  $\mathcal{A}_\ell^{(i)}$ . Since one patch can be sampled multiple times, the total size of the sampled set satisfies  $|\mathcal{A}_\ell^{(i)}| \leq N$ .

Each query vector  $q_\ell^{(i)}$  then exclusively attends to the visual features in the sampled region and adds to itself. In the multi-head cross-attention, the attention score on the image for each head  $j$  is calculated as

$$\alpha_{xy}^j = \frac{\exp\left(W_j^Q q_\ell^{(i)} \cdot W_j^K \mathbf{V}_{xy}^{(\lambda)} / d\right)}{\sum_{(x', y') \in \mathcal{A}_\ell^{(i)}} \exp\left(W_j^Q q_\ell^{(i)} \cdot W_j^K \mathbf{V}_{x'y'}^{(\lambda)} / d\right)}$$

for  $(x, y) \in \mathcal{A}_\ell^{(i)}$ , and 0 elsewhere<sup>2</sup>. The output of head  $j$  attention is

$$H_j = \sum_{(x', y') \in \mathcal{A}_\ell^{(i)}} \alpha_{x'y'}^j W_j^V \mathbf{V}_{x'y'}^{(\lambda)}.$$

The query is then updated by combining the heads and adding to itself:

$$q_{\ell+1}^{(i)} = q_\ell^{(i)} + [H_1, \dots, H_h] W^O.$$

We apply the same process for all query vectors  $q_\ell^{(1)}, \dots, q_\ell^{(m)}$ , followed by a layer normalization on the updated query ensemble before advancing to the next step.

**Step 3. Inter-query attention** After all the queries go through the Boltzmann attention sampling process, we apply a self-attention block such that the information is shared

<sup>1</sup>For computational efficiency, we sample from a Bernoulli distribution with probability  $1 - (1 - p(x, y; q_\ell^{(i)}))^N$  for each  $(x, y)$  in parallel as an approximation.

<sup>2</sup>We used the equivalent PyTorch attention masking feature in practice.

among themselves and with the text embeddings (to the right of the Boltzmann attention sampling box in Fig. 1):

$$\text{FFN}(\text{LayerNorm}([\mathbf{Q}_{\ell+1}, \mathbf{T}_\ell] + \text{SelfAttn}[\mathbf{Q}_{\ell+1}, \mathbf{T}_\ell])). \quad (6)$$

Again, we split out the  $\mathbf{Q}$  part before going through the feed-forward network layer. Here  $\mathbf{T}_\ell$  is the text embedding from the previous layer. The updated query embeddings and text embeddings are fed into the next *BoltzFormer* block.

### 3.3. PiGMA Query Aggregation

After  $L$  blocks of Boltzmann attention sampling, we obtain  $m$  finalized latent query vectors  $q_L^{(1)}, \dots, q_L^{(m)}$ . By applying the MLP transformation in Eq. (3) and estimating pixel-wise confidence score using Eq. (1), each query yields a mask prediction. In this work we use the PiGMA module illustrated in Fig. 3 to aggregate the mask predictions from multiple queries. The aggregated prediction combines the following two components.

**Query Ensemble Prediction** As the  $m$  predicted masks are the final pixel-wise confidence estimation, this component is simply the average of the mask predictions:

$$M = \frac{1}{m} \sum_{i=1}^m \text{MLP}(q_L^{(i)}) \cdot \mathbf{S}. \quad (7)$$

**Pixel-Grounded Correction** To better address the intrinsic randomness in the query predictions, we apply a lightweight two-layer convolutional network to the mask predictions, grounding on the original image pixels to give a high-resolution correction to the ensemble prediction. We illustrate the architecture in Figure 3.

The final output from PiGMA is the average of these two components. We further apply a pixel-wise sigmoid transformation to obtain a probabilistic mask prediction. The final mask prediction is supervised using the sum of the Dice loss [19] and binary cross-entropy loss.

### 3.4. Remarks

We finish this section with a few technical remarks.

- The goal of *BoltzFormer* is to reduce the attention region by first “guessing” on a learnable probability distribution. Each “guess” doesn’t need to be perfect, as there are multiple queries and rounds. The more relevant feature in each sampled set will be picked out by the cross-attention block efficiently, and shifts the updated query to focus more on those regions. Compared to standard attention which tries to focus on the desired feature only through optimizing on the massive number of tokens, sampling plus attention relieves the learning burden when the target region is very small.

- When *BoltzFormer* advances to the next round, features sampled in the previous round that are more relevant will be amplified through cross-attention. As the attention output is added to the original query vector, the next round’s Boltzmann distribution, estimated by the updated query vector, will more focus on the relevant features. Based on this mechanism, it is beneficial to spread out the sampling distribution in the early layers, reducing the likelihood of omitting any relevant features. The annealing temperature scheduling is designed to balance the exploration and exploitation.
- The ensemble of multiple queries not only diversify the exploration in Boltzmann sampling, but also boosts the final performance by their inter-communication through the self-attention layers. Once one of the queries get closer to the desired feature, all other queries can update towards the desired state.

## 4. Experiments

In order to evaluate the effectiveness of *BoltzFormer*, we conducted extensive experiments on seven public image segmentation datasets from Medical Segmentation Decathlon (MSD) [1], LIDC-IDRI [2] and AMOS22 [13]. We used the GPT-4 enriched data from BiomedParse<sup>3</sup> [29] to evaluate text prompt segmentation for the targets in these datasets. Example prompts include “right kidney in abdominal MRI” and “neoplasm in lung CT”. We ensure each of these datasets contain segmentation object types that are smaller than 1% of the image size in terms of area. The total benchmark suite covers a wide range of object sizes from below 0.002% to over 20% of image area, crossing four orders of magnitude. We provide detailed information in the Appendix.

### 4.1. Baselines

We compared *BoltzFormer* with three categories of baseline implementations.

**Segmentation FM decoder comparison:** We took the transformer decoder architectures of SOTA promptable image segmentation foundation models (FM), including SAM [14] (ICCV 2023), SEEM [33] (NeurIPS 2024), and the recent SAM 2 [20] (image version). To compare with *BoltzFormer* in the same text prompt setting, we customized SAM and SAM 2 to take in text embeddings using UniCL [27] as the language encoder. For image backbone, we used the Hiera [4, 22] model with masked autoencoder (MAE) pre-training [11], following the implementation in SAM 2 [20]. We compared the decoders in settings with different backbone configurations (Hiera-S and Hiera-BP). To test the compatibility of *BoltzFormer* with differ-

<sup>3</sup>We note that the processed variants are different from the original versions in that the images are in 2D and the split definition could be different.

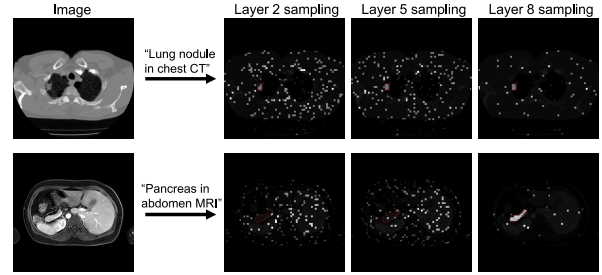


Figure 4. Examples of Boltzmann sampling from the intermediate layers during inference. For each image and text prompt, the queries only attend to the samples patches at each layer. The dark region is completely masked out in that layer. Boundaries of the ground truth object is marked in red.

ent backbone architectures, we also implemented an additional experiment using the Focal-L [26] backbone initialized from SEEM [33]. The pixel decoder architecture follows [7, 32, 33]. For all decoder-backbone combinations, we trained on the entirety of the benchmark suite jointly.

**Pre-trained foundation model comparison:** We took the weights of the state-of-the-art biomedical image foundation model BiomedParse [29] for comparison. BiomedParse takes in text prompt and performs segmentation for objects in medical images. The model was not further fine-tuned exclusively on the benchmark suite in this paper.

**Expert model comparison:** We used nnU-Net [12] as the expert model baseline. We trained 35 nnU-Net models in fully supervised setting performing binary segmentation for each object type in each dataset, without text prompting.

### 4.2. Results

Table 1 shows the Dice score evaluation of *BoltzFormer* compared with all the baseline models. Holding the image backbone constant, *BoltzFormer* outperformed all other segmentation FM decoders in mean Dice score averaged across the benchmark suite. The average performance improvements against the baseline decoders are: 12.4% against SAM, 12.6% against SAM 2, and 2.1% against SEEM. On individual benchmarks, *BoltzFormer* won over all baselines in most cases. In pre-trained model comparison, *BoltzFormer* outperformed BiomedParse on average and on each individual dataset. *BoltzFormer* also outperformed nnU-Net with 35 task-specific expert models. Lastly, *BoltzFormer* on the FocalL backbone shows dominant performance across the benchmark suite.

In terms of failure analysis, the ratio of failure cases where the model completely missed the target was estimated at 1.4%. Common failure examples are: 1. extremely small targets (e.g. a few pixels), 2. low contrast, 3. presence of other plausible objects.

Table 1. Evaluation results on segmentation benchmarks measured in mean Dice score (%). The first three sections are baseline models of the three categories. We present results of *BoltzFormer* in the last section. For *BoltzFormer* and the segmentation FM decoder baselines, we present each implementation as “DECODER+BACKBONE”. We mark each baseline decoders implementation with “text” to emphasize that they were all customized to take text prompts using the exact same language encoder as *BoltzFormer*. We mark the highest scoring model with **bold** in each column. We use underline to denote the best model under the same backbone size (e.g, S, BP).

Method	Avg.	LIDC	AMOS-CT	AMOS-MRI	MSD-Lung	MSD-Panc.	MSD-HepVes	MSD-Colon
<i>Expert models trained for each class in each dataset separately</i>								
nnU-Net	67.3	64.8	85.0	85.2	60.2	52.4	61.3	62.4
<i>Pre-trained biomedical foundation model</i>								
BiomedParse	73.0	73.8	91.9	87.6	66.1	60.2	64.8	66.4
<i>Segmentation FM decoders trained on this benchmark suite with custom text encoders and backbones</i>								
SAM+Heira-S (text)	67.0	67.1	88.4	83.9	61.6	55.1	61.2	52.0
SAM+Heira-BP (text)	64.9	62.8	86.7	81.2	57.2	51.4	60.8	54.0
SAM2+Heira-S (text)	65.6	65.4	88.2	82.6	59.8	52.8	59.8	50.6
SAM2+Heira-BP (text)	66.1	63.2	88.1	82.0	64.2	52.9	60.1	51.6
SEEM+Heira-S (text)	71.5	72.1	91.1	88.2	65.9	61.4	63.9	58.0
SEEM+Heira-BP (text)	73.8	72.9	92.0	89.3	69.3	<b>64.6</b>	65.7	63.3
<i>BoltzFormer (our method) trained on this benchmark suite with custom text encoders and backbones</i>								
BoltzFormer+Heira-S	<u>73.8</u>	<u>73.3</u>	<u>91.3</u>	<u>88.7</u>	<u>70.4</u>	<u>63.7</u>	<u>64.4</u>	<u>65.2</u>
BoltzFormer+Heira-BP	<u>74.5</u>	<u>73.6</u>	<u>92.0</u>	<u>89.3</u>	<b>71.4</b>	61.0	<u>66.7</u>	<b>66.7</b>
BoltzFormer+FocalL	<b>75.2</b>	<b>75.4</b>	<b>92.7</b>	<b>90.2</b>	70.2	64.0	<b>67.0</b>	<b>66.7</b>

### 4.3. Performance on small objects

To show the advantage of *BoltzFormer* in segmenting small objects, we filtered the segmentation examples into small and large groups with the threshold at 1% of the total image area. Table 2 shows the performance stratified by objects size, where *BoltzFormer* significantly outperformed all other baselines on small objects. Interestingly, we noticed that while *BoltzFormer* was leading on the large object group as well, the gap between *BoltzFormer* and the best competing method on large objects is very small, proving that the improvement from our approach was mainly contributed by the small objects.

Table 2. Dice score (with std) on small objects ( $< 1\%$  image area), large objects ( $\geq 1\%$  image area), and all objects. We calculated the average Dice score for each size group on each dataset in the benchmark suite, and reported the dataset average weighted by the ratio of the corresponding size group in each dataset.

	SAM	SAM2	SEEM	BoltzFormer
Small	64.5 (0.52)	62.1 (0.53)	68.9 (0.50)	<b>71.4 (0.44)</b>
Large	82.3 (0.57)	82.3 (0.57)	87.1 (0.36)	<b>87.5 (0.35)</b>
All	67.1 (0.46)	65.0 (0.46)	71.5 (0.44)	<b>73.7 (0.38)</b>

### 4.4. Visualization of Boltzmann attention sampling

In Fig. 4 we show the two examples of Boltzmann attention sampling during text prompt segmentation inference. The query only attends to the visual features on the sampled

patches. The sampling is spread out at the earlier layers, for the model to explore the image features. In the middle layers, *BoltzFormer* begins to exhaust the features in the target region, while continuing to explore other parts of the image. The sampling is highly concentrated on the target regions when getting close to the last layer to refine the prediction with the most relevant features.

Note that in the second example, the query didn’t attend to any feature from the target region until layer 5, however, after that the model quickly focused on the target region.

## 5. Ablation studies

We conducted thorough ablation studies for all newly introduced components in *BoltzFormer* to examine their effectiveness. We used Heiera-S as the backbone, and held all non-ablated parts constant for all experiments. Standard deviation estimates are provided in parentheses.

### 5.1. Boltzmann attention sampling

To show the effectiveness of Boltzmann attention sampling in attention masking, we compared with the standard full attention, as well as fixed threshold masking following [7, 33]. Table 3 shows the average Dice score evaluated across the benchmark suite, where Boltzmann attention sampling showed significant advantage over full attention and fixed threshold masking.

Table 3. Average Dice score (%) when using regular full attention, fixed attention mask threshold, and Boltzmann attention sampling.

Full attention	0.5 threshold	Boltz. sampling (ours)
71.2 (0.43)	72.4 (0.41)	<b>73.7 (0.38)</b>

## 5.2. Temperature for sampling

Temperature is the critical parameter in balancing exploration vs. exploitation and controlling the annealing behavior. In Table 4 we experimented with different base temperatures in the layer-decay formula  $\tau_\ell = \frac{\tau_0}{\ell+1}$ . We found that a balanced value  $\tau_0 = 1$  yielded the best performance. The performance dropped significantly when the temperature is too high, as the model explored for too long and couldn't exploit the most relevant features.

Table 4. Average Dice score (%) when changing the base layer temperature in Boltzmann sampling.

Temp.	$\tau_0 = 0.25$	$\tau_0 = 0.5$	$\tau_0 = 1$	$\tau_0 = 2$
Dice	73.6 (0.40)	73.0 (0.43)	<b>73.7 (0.38)</b>	72.2 (0.42)

## 5.3. Sampling size

We experimented with the number of samples drawn by each query in each layer, measured as a percentage of the total number of visual features  $N_v$  in that layer. In Table 5 we observed that with as few as 5% features *BoltzFormer* is able to deliver satisfactory performance, and 10% sampling gave the best performance. Further increasing the sample size didn't help with the model performance.

Table 5. Average Dice score (%) when changing the number of independent samples in Boltzmann sampling.  $N_v$  refers to the total number of visual features in that layer.

# sample	5% $N_v$	10% $N_v$	20% $N_v$	50% $N_v$
Dice	72.9 (0.40)	<b>73.7 (0.38)</b>	72.4 (0.42)	73.6 (0.40)

## 5.4. Number of queries

One key component in *BoltzFormer* is the design of multiple queries which perform independent distribution estimation and sampling. The self-attention layer after each Boltzmann attention sampling layer communicates the useful features across the ensemble. From Table 6 we observed that as few as 10 queries is enough for best performance, and there was no notable difference when further increasing the number of queries. When there is no ensemble (only 1 query) the performance dropped notably.

Table 6. Average Dice score (%) when changing the number of queries in *BoltzFormer*.

# queries	1	10	32	101
Dice	72.8 (0.42)	<b>73.8 (0.38)</b>	<b>73.8 (0.38)</b>	73.7 (0.38)

## 5.5. Text-conditional query prior

The self-attention layer before the first Boltzmann attention sampling block helps the queries to initialize based on the semantic from the text prompt. Table 7 illustrates the performance gain from text-conditioning (Eq. (4)).

Table 7. Average Dice score (%) when using unconditioned query prior v.s. using query prior conditioned on input text.

Unconditioned prior	Text-conditioned prior
72.3 (0.44)	<b>73.7 (0.38)</b>

## 5.6. PiGMA module

The PiGMA module at the end of the model provides a non-linear aggregation of the different predictions from the multiple queries by grounding on the original image. Table 8 shows the improvement from pixel grounded correction.

Table 8. Average Dice score (%) when using query ensemble prediction only v.s. adding high resolution pixel grounded correction.

Query ensemble only	With pixel grounded correction
73.2 (0.43)	<b>73.7 (0.38)</b>

## 6. Conclusion

Detecting and segmenting small objects remains a significant challenge in holistic image analysis. In this paper, we introduced *BoltzFormer* for detecting and segmenting small objects by learning to dynamically sample sparse areas for focused self-attention using a Boltzmann distribution with an annealing temperature schedule. Effectively, *BoltzFormer* adopts a form of reinforcement learning by maintaining layerwise representation (state) and selecting the sparse subset of the image (action) through Boltzmann sampling (policy). In thorough evaluation on standard image analysis datasets with small objects, *BoltzFormer* substantially outperforms prior best methods in segmentation accuracy, while reducing self-attention computation by an order of magnitude. Future work will focus on enhancing accuracy and efficiency, as well as expanding applications to additional modalities and object types.



## References

- [1] Michela Antonelli, Annika Reinke, Spyridon Bakas, Keyvan Farahani, Annette Kopp-Schneider, Bennett A Landman, Geert Litjens, Bjoern Menze, Olaf Ronneberger, Ronald M Summers, et al. The medical segmentation decathlon. *Nature communications*, 13(1):4128, 2022. 6
- [2] Samuel G Armato III, Geoffrey McLennan, Luc Bidaut, Michael F McNitt-Gray, Charles R Meyer, Anthony P Reeves, Binsheng Zhao, Denise R Aberle, Claudia I Henschke, Eric A Hoffman, et al. The lung image database consortium (LIDC) and image database resource initiative (IDRI): a completed reference database of lung nodules on CT scans. *Medical physics*, 38(2):915–931, 2011. 6
- [3] Iz Beltagy, Matthew E Peters, and Arman Cohan. Longformer: The long-document transformer. *arXiv preprint arXiv:2004.05150*, 2020. 3
- [4] Daniel Bolya, Chaitanya Ryali, Judy Hoffman, and Christoph Feichtenhofer. Window attention is bugged: How not to interpolate position embeddings. In *The Twelfth International Conference on Learning Representations*. 6
- [5] Nicolas Carion, Francisco Massa, Gabriel Synnaeve, Nicolas Usunier, Alexander Kirillov, and Sergey Zagoruyko. End-to-end object detection with transformers. In *European conference on computer vision*, pages 213–229. Springer, 2020. 3
- [6] Bowen Cheng, Alex Schwing, and Alexander Kirillov. Pixel classification is not all you need for semantic segmentation. *Advances in neural information processing systems*, 34:17864–17875, 2021. 3
- [7] Bowen Cheng, Ishan Misra, Alexander G Schwing, Alexander Kirillov, and Rohit Girdhar. Masked-attention mask transformer for universal image segmentation. In *Proceedings of the IEEE/CVF conference on computer vision and pattern recognition*, pages 1290–1299, 2022. 1, 3, 4, 6, 7
- [8] Rewon Child, Scott Gray, Alec Radford, and Ilya Sutskever. Generating long sequences with sparse transformers. *arXiv preprint arXiv:1904.10509*, 2019. 3
- [9] Ross Girshick. Fast r-cnn. In *Proceedings of the IEEE international conference on computer vision*, pages 1440–1448, 2015. 3
- [10] Kaiming He, Georgia Gkioxari, Piotr Dollár, and Ross Girshick. Mask R-CNN. In *Proceedings of the IEEE international conference on computer vision*, pages 2961–2969, 2017. 3
- [11] Kaiming He, Xinlei Chen, Saining Xie, Yanghao Li, Piotr Dollár, and Ross Girshick. Masked autoencoders are scalable vision learners. In *Proceedings of the IEEE/CVF Conference on Computer Vision and Pattern Recognition*, pages 16000–16009, 2022. 6
- [12] Fabian Isensee, Paul F Jaeger, Simon AA Kohl, Jens Petersen, and Klaus H Maier-Hein. nnU-Net: a self-configuring method for deep learning-based biomedical image segmentation. *Nature methods*, 18(2):203–211, 2021. 6
- [13] Yuanfeng Ji, Haotian Bai, Chongjian Ge, Jie Yang, Ye Zhu, Ruimao Zhang, Zhen Li, Lingyan Zhanng, Wanling Ma, Xiang Wan, et al. Amos: A large-scale abdominal multi-organ benchmark for versatile medical image segmentation. *Advances in neural information processing systems*, 35:36722–36732, 2022. 6
- [14] Alexander Kirillov, Eric Mintun, Nikhila Ravi, Hanzi Mao, Chloe Rolland, Laura Gustafson, Tete Xiao, Spencer Whitehead, Alexander C Berg, Wan-Yen Lo, et al. Segment anything. In *Proceedings of the IEEE/CVF International Conference on Computer Vision*, pages 4015–4026, 2023. 1, 3, 6
- [15] Ho Hin Lee, Yu Gu, Theodore Zhao, Yanbo Xu, Jianwei Yang, Naoto Usuyama, Cliff Wong, Mu Wei, Bennett A. Landman, Yuankai Huo, Alberto Santamaria-Pang, and Hoi-fung Poon. Foundation models for biomedical image segmentation: A survey, 2024. 1
- [16] I Loshchilov. Decoupled weight decay regularization. *arXiv preprint arXiv:1711.05101*, 2017. 1
- [17] Jun Ma, Yuting He, Feifei Li, Lin Han, Chenyu You, and Bo Wang. Segment anything in medical images. *Nature Communications*, 15(1):654, 2024. 1, 3
- [18] Jun Ma, Sumin Kim, Feifei Li, Mohammed Baharoon, Reza Asakereh, Hongwei Lyu, and Bo Wang. Segment anything in medical images and videos: Benchmark and deployment, 2024. 3
- [19] Fausto Milletari, Nassir Navab, and Seyed-Ahmad Ahmadi. V-Net: Fully convolutional neural networks for volumetric medical image segmentation. In *2016 fourth international conference on 3D vision (3DV)*, pages 565–571. IEEE, 2016. 5
- [20] Nikhila Ravi, Valentin Gabeur, Yuan-Ting Hu, Ronghang Hu, Chaitanya Ryali, Tengyu Ma, Haitham Khedr, Roman Rädle, Chloe Rolland, Laura Gustafson, et al. Sam 2: Segment anything in images and videos. *arXiv preprint arXiv:2408.00714*, 2024. 1, 3, 6
- [21] Olaf Ronneberger, Philipp Fischer, and Thomas Brox. U-Net: Convolutional networks for biomedical image segmentation. In *Medical Image Computing and Computer-Assisted Intervention—MICCAI 2015: 18th International Conference, Munich, Germany, October 5–9, 2015, Proceedings, Part III 18*, pages 234–241. Springer, 2015. 3
- [22] Chaitanya Ryali, Yuan-Ting Hu, Daniel Bolya, Chen Wei, Haoqi Fan, Po-Yao Huang, Vaibhav Aggarwal, Arkabandhu Chowdhury, Omid Poursaeed, Judy Hoffman, et al. Hiera: A hierarchical vision transformer without the bells-and-whistles. In *International Conference on Machine Learning*, pages 29441–29454. PMLR, 2023. 6
- [23] Peize Sun, Rufeng Zhang, Yi Jiang, Tao Kong, Chenfeng Xu, Wei Zhan, Masayoshi Tomizuka, Lei Li, Zehuan Yuan, Changhu Wang, et al. Sparse r-cnn: End-to-end object detection with learnable proposals. In *Proceedings of the IEEE/CVF conference on computer vision and pattern recognition*, pages 14454–14463, 2021. 3
- [24] A Vaswani. Attention is all you need. *Advances in Neural Information Processing Systems*, 2017. 1
- [25] Hallee E Wong, Marianne Rakic, John Guttag, and Adrian V Dalca. Scribbleprompt: fast and flexible interactive segmentation for any biomedical image. In *European Conference on Computer Vision*, pages 207–229. Springer, 2024. 1

- [26] Jianwei Yang, Chunyuan Li, Xiyang Dai, and Jianfeng Gao. Focal modulation networks. *Advances in Neural Information Processing Systems*, 35:4203–4217, 2022. [6](#)
- [27] Jianwei Yang, Chunyuan Li, Pengchuan Zhang, Bin Xiao, Ce Liu, Lu Yuan, and Jianfeng Gao. Unified contrastive learning in image-text-label space. In *Proceedings of the IEEE/CVF Conference on Computer Vision and Pattern Recognition*, pages 19163–19173, 2022. [6](#)
- [28] Hao Zhang, Feng Li, Huaizhe Xu, Shijia Huang, Shilong Liu, Lionel M Ni, and Lei Zhang. Mp-former: Mask-piloted transformer for image segmentation. In *Proceedings of the IEEE/CVF Conference on Computer Vision and Pattern Recognition*, pages 18074–18083, 2023. [1](#), [3](#)
- [29] Theodore Zhao, Yu Gu, Jianwei Yang, Naoto Usuyama, Ho Hin Lee, Sid Kiblawi, Tristan Naumann, Jianfeng Gao, Angela Crabtree, Jacob Abel, Christine Moungh-Wen, Brian Piening, Carlo Bifulco, Mu Wei, Hoifung Poon, and Sheng Wang. A foundation model for joint segmentation, detection, and recognition of biomedical objects across nine modalities. *Nature Methods*, 2024. [1](#), [3](#), [6](#)
- [30] Jiayuan Zhu, Yunli Qi, and Junde Wu. Medical SAM 2: Segment medical images as video via segment anything model 2. *arXiv preprint arXiv:2408.00874*, 2024. [1](#)
- [31] Xizhou Zhu, Weijie Su, Lewei Lu, Bin Li, Xiaogang Wang, and Jifeng Dai. Deformable detr: Deformable transformers for end-to-end object detection. In *International Conference on Learning Representations*. [4](#)
- [32] Xueyan Zou, Zi-Yi Dou, Jianwei Yang, Zhe Gan, Linjie Li, Chunyuan Li, Xiyang Dai, Harkirat Behl, Jianfeng Wang, Lu Yuan, et al. Generalized decoding for pixel, image, and language. In *Proceedings of the IEEE/CVF Conference on Computer Vision and Pattern Recognition*, pages 15116–15127, 2023. [6](#)
- [33] Xueyan Zou, Jianwei Yang, Hao Zhang, Feng Li, Linjie Li, Jianfeng Wang, Lijuan Wang, Jianfeng Gao, and Yong Jae Lee. Segment everything everywhere all at once. *Advances in Neural Information Processing Systems*, 36, 2024. [1](#), [3](#), [6](#), [7](#)

# Boltzmann Attention Sampling for Image Analysis with Small Objects

## Supplementary Material

### A. Implementation details

#### A.1. Image encoder

We used Hiera or FocalNet as the image backbone. Both models outputs four scales of features with strides 4, 8, 16 and 32. The pixel decoder takes the multiscale backbone features to output multiscale visual features of resolution  $32 \times 32$ ,  $64 \times 64$ ,  $128 \times 128$  and  $256 \times 256$ . The multiscale visual features convolute to semantic map in resolution  $256 \times 256$ . *BoltzFormer* attends to multiscale visual features of resolution  $32 \times 32$ ,  $64 \times 64$  and  $128 \times 128$  in loops. We repeated the loop of the three scales in this order for three times, resulting in nine layers in total. The query vectors after the ninth layer was used for prediction.

#### A.2. Language encoder

We used UniCL as the language encoder for text prompts. The context length is 77. We input the full token embedding sequence to *BoltzFormer*.

#### A.3. Boltzmann sampling

In our main experiments, we used a sampling ratio of 10%, which means at each layer the number of independent trials is 10% of the total number of visual features of that scale. We used default base temperature  $\tau_0 = 1$ .

#### A.4. Training specifics

We used 32 NVIDIA A100 80GB GPUs for *BoltzFormer* training. We used batch size  $12 \times 32$  for Hiera-S and Hiera-BP backbones, and batch size  $8 \times 32$  for Focal-L backbone. During training we split out 20% from the training set for validation, and monitored the validation loss. We trained with early stopping based on validation loss for a maximum of 40 epochs. We used AdamW [16] as the optimizer with equal weighted Dice loss and pixel-wise binary cross-entropy loss. Selected training hyper-parameters based on validation loss for learning rates  $2 \times 10^{-5}$ ,  $4 \times 10^{-5}$ ,  $5 \times 10^{-5}$ ,  $1 \times 10^{-4}$ , and weight decays  $10^{-4}$ ,  $10^{-3}$ ,  $10^{-2}$ . We used learning rate  $2 \times 10^{-5}$  and weight decay  $10^{-2}$  for training *BoltzFormer*.

#### A.5. Data augmentation

We implemented random transformation for the images and ground truth masks. Each training example had 50% probability to be transformed. We randomly rotated the image and corresponding ground truth mask by  $0^\circ$ ,  $90^\circ$ ,  $180^\circ$ ,  $270^\circ$ . We randomly cropped the image and the corresponding ground truth mask by shifting the center

by  $\pm 10\%$  horizontally and vertically, and scaling by  $\pm 10\%$ . All random augmentation were uniformly sampled.

### B. Dataset details

We listed the object size statistics for all the benchmark datasets we used for evaluation in Table 9. The benchmark suite used in our study covered a wide range of object sizes, from 0.002% to 20% of the image area, crossing four orders of magnitudes. The majority of the object types in each dataset have mean object size less than 1% of the image area.

### C. Visualizations

#### C.1. Boltzmann sampling

We visualize the examples of Boltzmann attention sampling through the layers in *BoltzFormer*. In each layer, each query vector only attend to the sampled visual features visualized in the figures. We looped through the three scales of visual features for three times, resulting in nine layers in total. The shaded regions are completely invisible to the query in that layer. We show the Boltzmann sampling for the first query in the ensemble in these examples.

From Fig. 5, 6, 7 and 8 we can see that the sampling is wide spread during the early layers. The sampling began to concentrate towards the target region during the middle layers, while still exploring the other regions. At the final layers the sampling was highly concentrated on the target regions.

In Fig. 8 we show the Boltzmann sampling example for an object with size greater than 20% of the total image area. Because the sampling ratio is just 10%, it is impossible to cover all the visual features in the target region. *BoltzFormer* still works for objects with large sizes as the sampled visual features are enough to summarize the semantics of the object.

#### C.2. Segmentation result comparison

In Fig. 9 we visualize the segmentation results from the baseline models and *BoltzFormer*. All transformer decoders took in text prompts through the UniCL language encoder. The backbone was fixed as Hiera-S for all the models. We visualize the segmentation masks in green, and outline the boundary of the ground truth target in red for reference.

We can see that *BoltzFormer* consistently delivered accurate segmentation, while the baseline models could miss the target completely when the object is very small (lung nodule and tumor, pancreas tumor). When the object is very large, *BoltzFormer* still output accurate segmentation result.

Table 9. Statistics about the benchmark datasets. We listed all the object types for segmentation in each of the datasets, along with the mean, median, min and max of the object size as a ratio to the total image area.

Dataset	Object type	Area mean (%)	Area median (%)	Area min (%)	Area max (%)	Support
LIDC-IDRI	nodule	0.059	0.029	0.002	0.802	1733
MSD-Lung	tumor	0.283	0.200	0.011	1.062	242
MSD-Pancreas	tumor	0.629	0.295	0.018	5.106	575
MSD-Pancreas	pancreas	0.567	0.465	0.029	2.431	1635
MSD-Hepatic Vessel	tumor	0.535	0.281	0.005	3.652	918
MSD-Hepatic Vessel	vessel	0.211	0.178	0.017	0.878	2204
MSD-Colon	tumor	0.472	0.341	0.036	2.287	245
AMOS22-CT	adrenal gland	0.185	0.169	0.037	0.503	420
AMOS22-CT	esophagus	0.142	0.102	0.018	1.189	1964
AMOS22-CT	postcava	0.237	0.218	0.034	0.751	4105
AMOS22-CT	spleen	1.952	1.752	0.142	6.587	1587
AMOS22-CT	right adrenal gland	0.087	0.073	0.010	0.304	571
AMOS22-CT	left kidney	1.194	1.206	0.065	2.649	1776
AMOS22-CT	kidney	2.509	2.473	0.334	4.798	1465
AMOS22-CT	duodenum	0.497	0.425	0.036	2.816	1677
AMOS22-CT	bladder	2.216	1.780	0.161	7.851	864
AMOS22-CT	gallbladder	0.664	0.490	0.035	2.946	712
AMOS22-CT	liver	7.896	7.285	0.694	21.498	4648
AMOS22-CT	right kidney	1.171	1.191	0.052	2.295	1649
AMOS22-CT	left adrenal gland	0.091	0.082	0.004	0.279	635
AMOS22-CT	pancreas	0.818	0.653	0.071	3.016	1345
AMOS22-CT	stomach	3.222	2.724	0.165	11.275	1837
AMOS22-CT	aorta	0.433	0.281	0.051	3.957	4409
AMOS22-MRI	adrenal gland	0.115	0.111	0.048	0.216	49
AMOS22-MRI	esophagus	0.064	0.058	0.022	0.167	134
AMOS22-MRI	postcava	0.135	0.116	0.033	0.351	463
AMOS22-MRI	spleen	1.353	1.296	0.130	2.707	197
AMOS22-MRI	right adrenal gland	0.056	0.053	0.011	0.157	56
AMOS22-MRI	left kidney	0.917	0.955	0.151	1.774	237
AMOS22-MRI	kidney	1.909	1.913	0.637	3.027	198
AMOS22-MRI	duodenum	0.280	0.264	0.075	0.860	201
AMOS22-MRI	gallbladder	0.407	0.366	0.046	0.914	75
AMOS22-MRI	liver	6.060	5.950	0.891	11.907	304
AMOS22-MRI	right kidney	0.882	0.935	0.146	1.467	224
AMOS22-MRI	left adrenal gland	0.051	0.045	0.020	0.109	84
AMOS22-MRI	pancreas	0.583	0.522	0.106	1.626	195
AMOS22-MRI	stomach	1.054	0.975	0.224	2.687	216
AMOS22-MRI	aorta	0.179	0.173	0.075	0.355	490



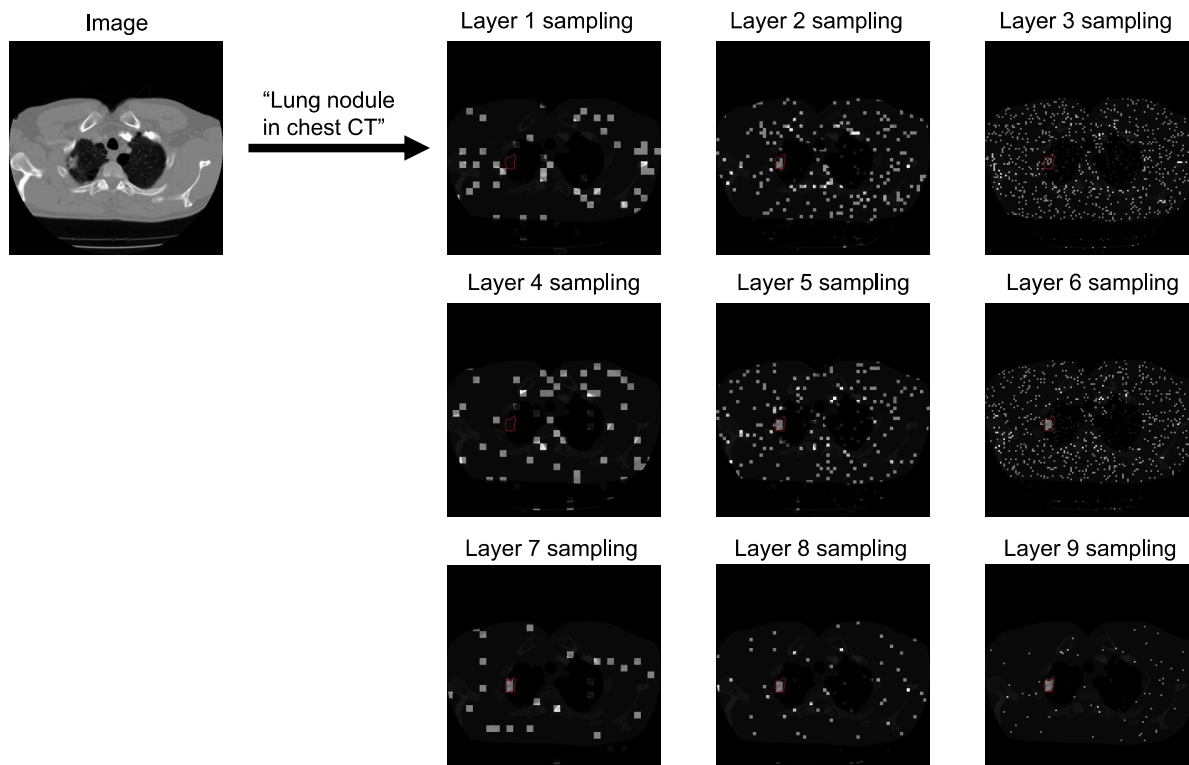


Figure 5. Boltzmann sampling example for lung nodule in chest CT. The sample patches are bright with target region circled in red.

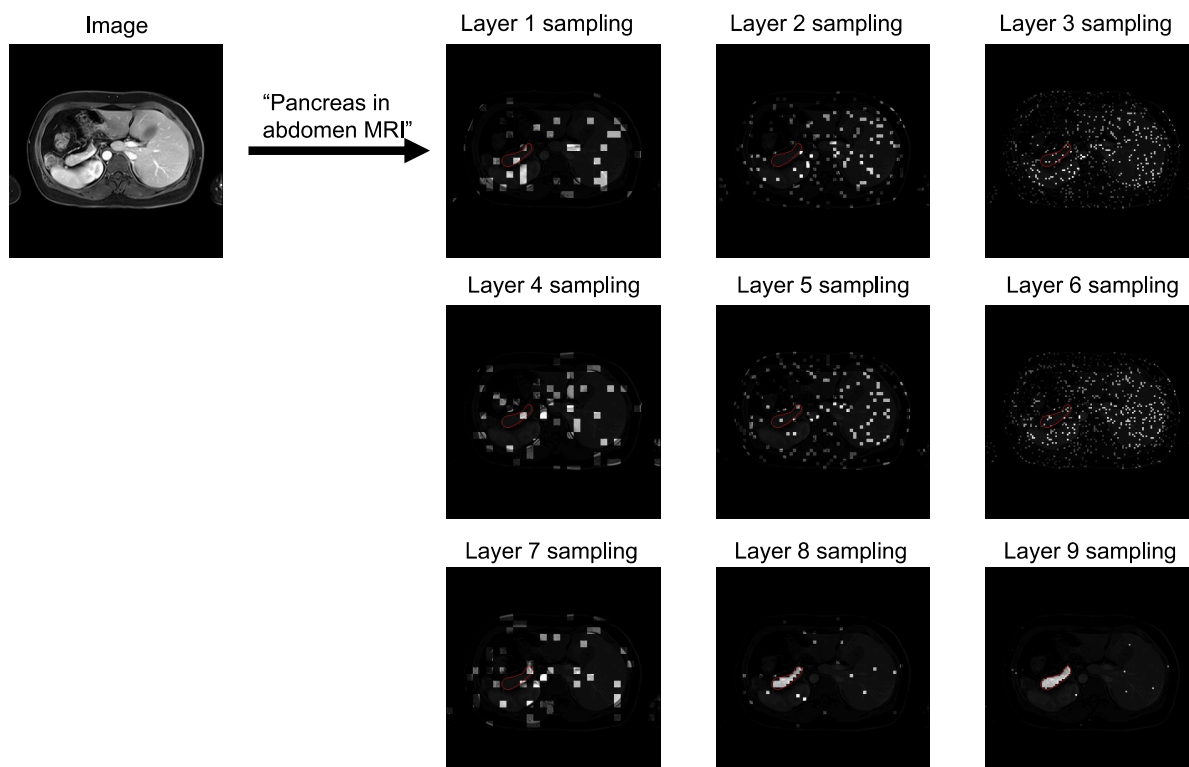


Figure 6. Boltzmann sampling example for pancreas in abdomen MRI. The sample patches are bright with target region circled in red.

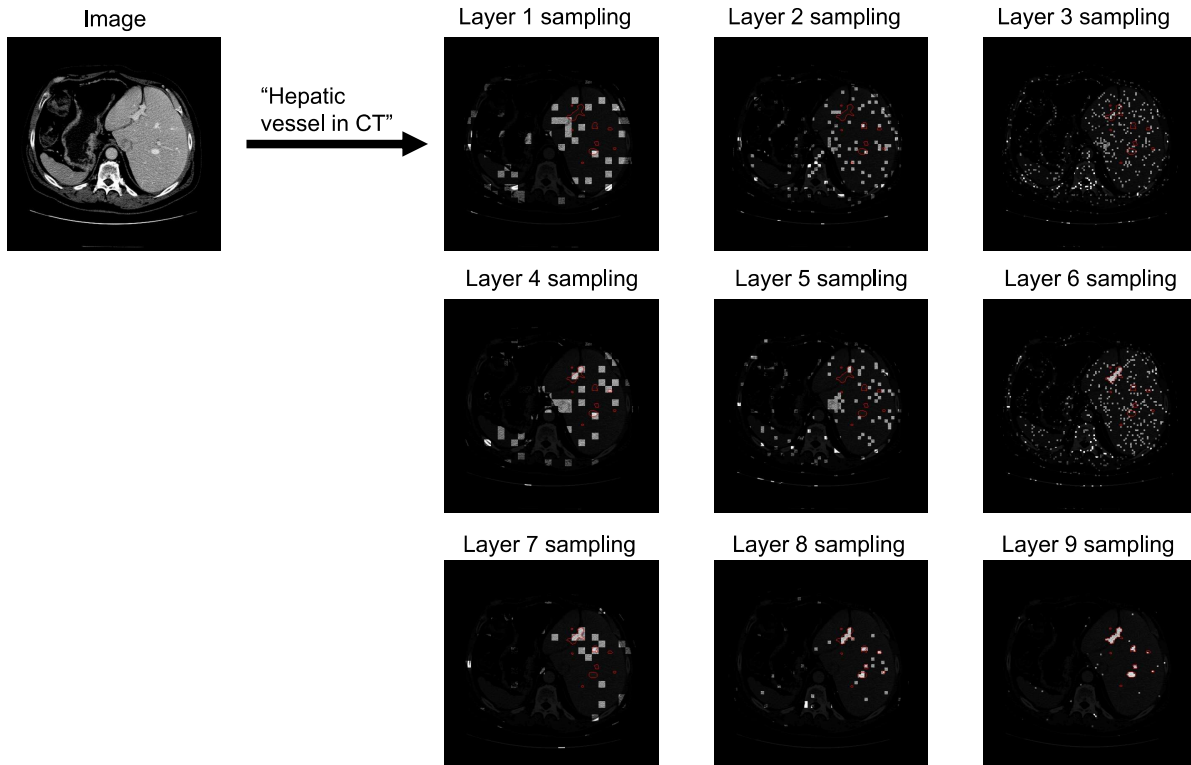


Figure 7. Boltzmann sampling example for hepatic vessel in CT. The sample patches are bright with target region circled in red.

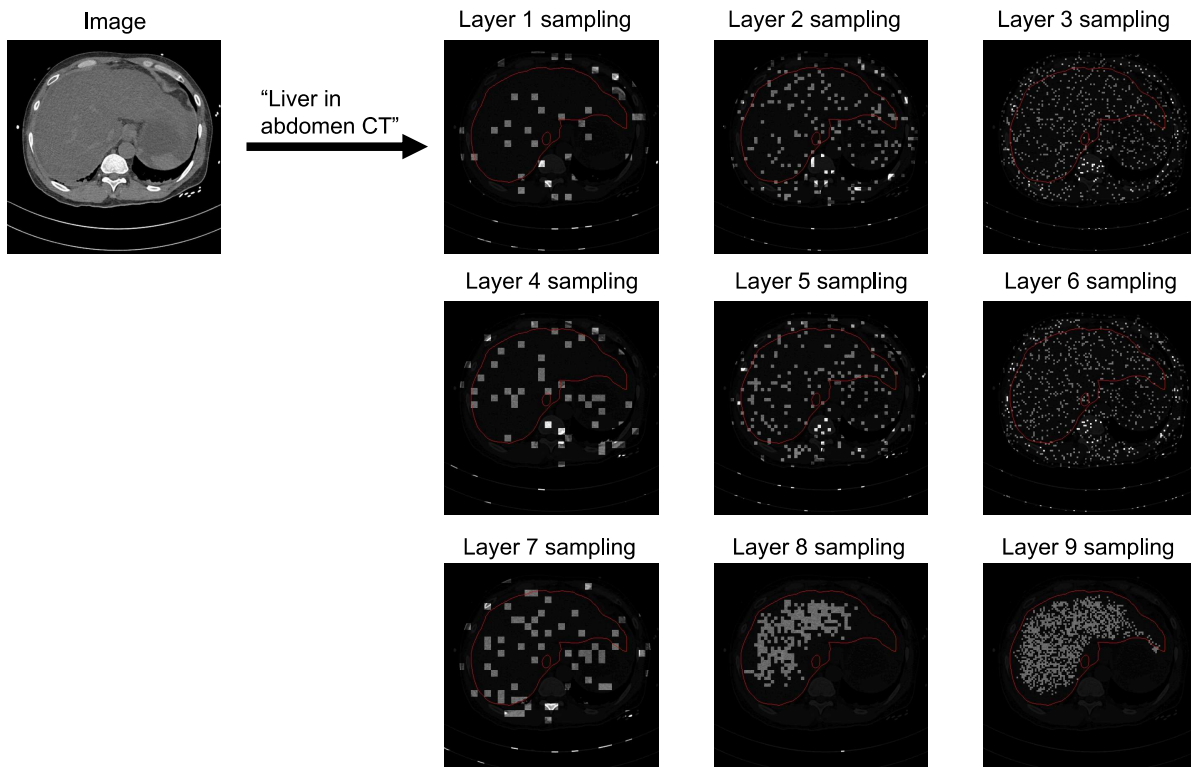


Figure 8. Boltzmann sampling example for liver in abdomen CT. The sample patches are bright with target region circled in red.

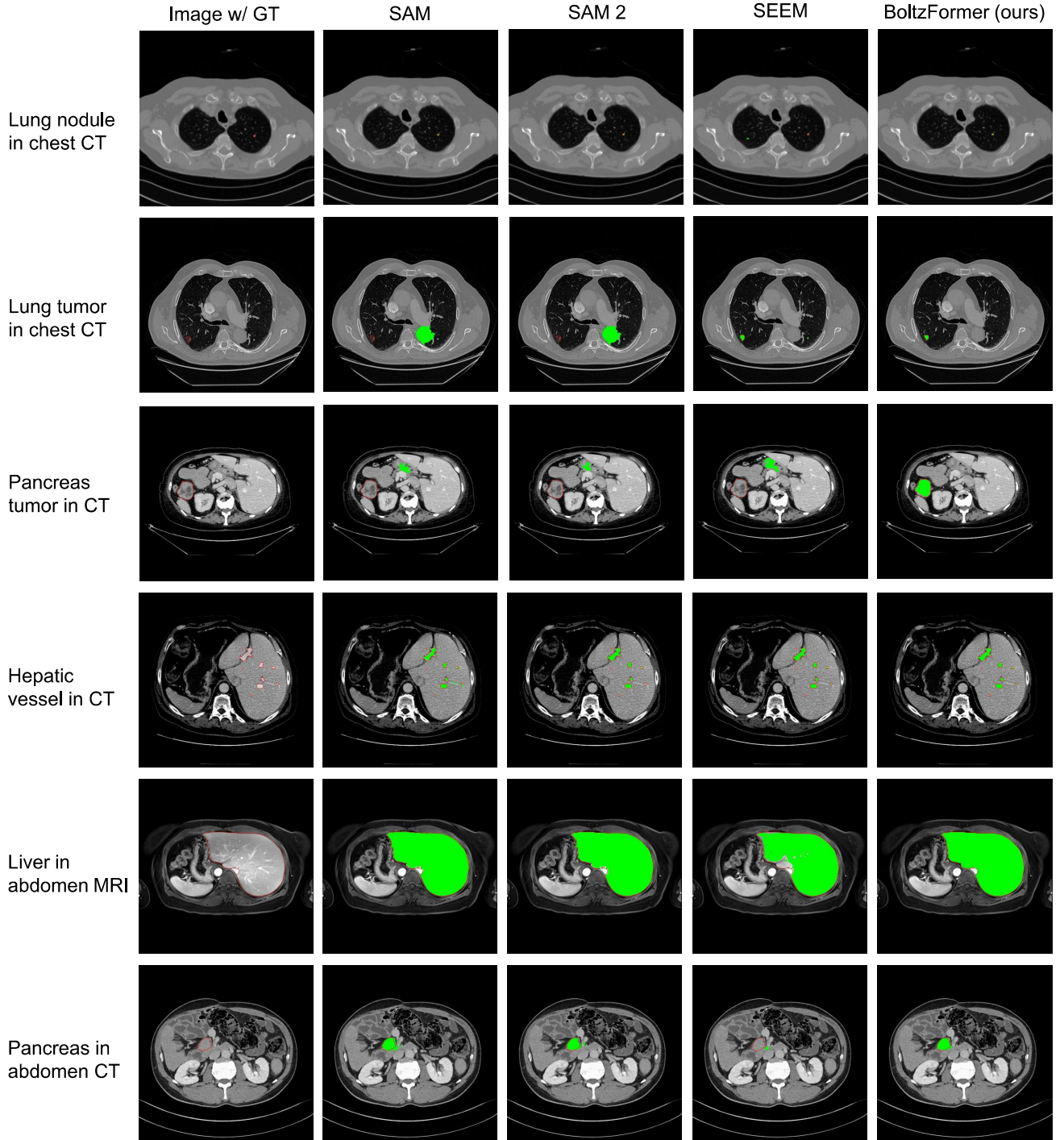


Figure 9. Segmentation prediction examples for baseline decoders and *BoltzFormer*. Target region is circled in red. Predicted segmentation masks are covered by green. We used the text prompts for all the models. The image backbone is fixed to Hiera-S for all the decoder models.